



Carrier concentration and in-plane mobility in both non-intentionally and Si-doped InAsSb and InAs/InAsSb type-II superlattice materials for space-based infrared detectors

Christian P. Morath^{1*}, Lilian K. Casias^{2,3}, Gilberto A. Umana-Membreno⁴, Preston T. Webster¹, Perry C. Grant¹, Diana Maestas¹, Vincent M. Cowan¹, Lorenzo Faraone⁴, Sanjay Krishna⁵, Ganesh Balakrishnan³

¹U.S. Air Force Research Lab Space Vehicles Directorate, 3550 Kirtland AFB, 427 Aberdeen Ave., NM 87117, USA

²Sandia National Laboratories, 1515 Eubank Blvd. SE, Albuquerque, NM 87185, USA

³Center for High Technology Materials, University of New Mexico, 1313 Goddard St. SE, Albuquerque, NM 87106, USA

⁴School of Electrical, Electronic, and Computer Engineering, The University of Western Australia, 25 Fairway, Crawley WA 6009, Australia

⁵Department of Electrical Engineering, The Ohio State University, 2015 Neil Ave., Columbus, OH 43210, USA

Article info

Article history:

Received 07 Oct. 2022

Received in revised form 20 Nov. 2022

Accepted 19 Dec. 2022

Available on-line 24 Feb. 2023

Keywords:

III-V infrared detectors;
Bulk InAsSb;
InAsSb/InAs superlattice;
Mobility;
Carrier concentration.

Abstract

The sensitivity of III-V-based infrared detectors is critically dependent upon the carrier concentration and mobility of the absorber layer, and thus, accurate knowledge of each is required to design structures for maximum detector performance. Here, measurements of the bulk in-plane resistivity, in-plane mobility, and carrier concentration as a function of temperature are reported for non-intentionally doped and Si-doped mid-wave infrared InAs_{0.91}Sb_{0.09} alloy and InAs/InAs_{0.65}Sb_{0.35} type-II superlattice materials grown on GaSb substrates. Standard temperature- and magnetic-field-dependent resistivity and the Hall measurements on mesa samples in the van der Pauw configuration are performed, and multi-carrier fitting and modelling are used to isolate transport of each carrier species. The results show that up to 5 carrier species of the surface, interface and bulk variety contribute to conduction, with bulk electron and hole mobility up to $2 \cdot 10^5$ cm²/V s and $8 \cdot 10^3$ cm²/V s, respectively and background dopant concentration levels were between 10^{14} and 10^{15} cm⁻³. The in-plane mobility temperatures dependence is determined and trends of each carrier species with temperature and dose are analysed.

1. Introduction

Mid-wave infrared (IR) space-sensing applications remain dominated by high performance mercury/cadmium/telluride (MCT) detectors, due to the material high absorption coefficient and the very long minority carrier lifetime. The recent introduction of fully depleted MCT detectors which follow Law 19 and their promise of improved high temperature performance guarantees that interest in MCT will continue for the foreseeable future [1, 2]. However, high-quality MCT still remains challenging to grow due to its unique growth requirement for high mercury vapour pressure [3]. Additionally, there is a

known lack of suppliers for high-quality large format CdZnTe substrate materials and environmental concerns regarding the use of Hg and Cd are also growing [4]. Moreover, as the cost of space lift continues to decrease [5], sensing satellite constellations will likely grow much larger in size [6] and may require larger numbers of focal plane arrays (FPAs) than can be accommodated by the arguably limited MCT manufacturing infrastructure (e.g., see section 7.6.2 of Ref. 7) or possibly relax the performance requirements sufficiently to allow substitutes. Hence, there remains interest in alternatives to MCT.

The leading alternative to MCT for mid-wave IR space-sensing are currently III-V-based barrier detector technologies, such as the nBn, employing either bulk InAsSb or InAs/InAsSb type-II superlattice (T2SL) absorber-

*Corresponding author at: christian.morath.2@spaceforce.mil

<https://doi.org/10.24425/opelre.2023.144554>

1896-3757/ Association of Polish Electrical Engineers (SEP) and Polish Academic of Sciences (PAS). Published by PAS
© 2023 The Author(s). This is an open access article under the CC BY license (<http://creativecommons.org/licenses/by/4.0/>).

ing layers. The nBn detector was first introduced well over a decade ago [8] and has progressed significantly since then, with dark currents now routinely within a factor of $10\times$ 'Rule 07' and quantum efficiency $> 50\%$ without an anti-reflection coating in the mid-wave IR [9,10]. However, higher performance is always desirable for space-sensing applications where detectors may operate in much lower background conditions. Additionally, space-sensing necessitates high tolerance to radiation-induced displacement damage [11], which is a concern for III-V materials given that their lifetime degradation rate from proton-irradiation is > 10 -times faster than MCT's [12].

Improving the overall performance and rad-tolerance of III-V nBn detectors will require continued advancement in design and material quality. For that to occur, accurate knowledge of carrier concentration and mobility, including their dependence on temperature, is required. Here, recent measurements of the bulk in-plane resistivity and mobility, and carrier concentration as a function of temperature are reported for non-intentionally doped and Si-doped mid-wave bulk $\text{InAs}_{0.91}\text{Sb}_{0.09}$ and $\text{InAs}/\text{InAs}_{0.65}\text{Sb}_{0.35}$ T2SL materials grown on GaSb substrates. These results are obtained by magneto-transport measurements in combination with multi-carrier fitting (MCF) and modelling. An analysis of the results and trends is also presented.

The paper is organized as follows. In section 2, a summary of relevant previous work is given. Section 3 describes the experimental methodology. Section 4 presents the measured results and provides some discussion. Finally, conclusions are made in section 5.

2. Background

An extended discussion of transport in III-V materials was given in Ref. 13 and only the most relevant works are cited in the following. An early work detailed magneto-transport in long-wave infrared (LWIR) n-type $\text{InAs}/\text{Ga}_{1-x}\text{In}_x\text{Sb}$ superlattices grown on GaAs substrates and showed multi-carrier conduction dominated by electrons, whose mobility was limited by interface roughness scattering, as well as the influence of roughness fluctuations on transport [14]. Following this, a study of transport in mid-wave infrared (MWIR) GaSb/InAs T2SLs grown on GaSb indicated that transport was dominated by the p-type substrate conduction; however, quantitative mobility spectrum analysis (QMSA) was able to resolve the conduction contribution of a single electron species in the superlattice by comparing results from substrate alone [15]. Another later study on transport in GaSb/InAs T2SLs grown on GaSb resolved this p-type substrate conduction issue by measuring at 20 K, where substrate conduction was frozen out, and confirmed in-plane mobilities were limited by interface roughness scattering [16]. Likewise, in another transport study on InAs/GaSb T2SLs, the substrate was physically removed to remove its influence and SL transport indicated a conductivity change from p- to n-type with temperature [17]. Finally, another study on GaSb/InAs T2SLs showed in-plane carrier mobility in n- and p-type samples was inversely proportional to carrier density, a consequence of screened interface roughness scattering [18].

The earliest transport study on InAs/InAsSb T2SL was performed by Brown *et al.* on a non-intentionally doped and Be-doped LWIR material [19]. These results examined the influence of dopant concentration on in-plane mobility, as well as different passivation treatments to mitigate surface conduction. A follow up study by Casias *et al.* on in-plane transport in MWIR, Be-doped InAsSb demonstrated a method to identify the bulk hole carrier species using conductivity measurements as function of film thickness and identify the surface electron species by dipping samples in NaClO and observing conduction changes [20].

Lastly, for IR detector applications, transport by minority carriers in the out-of-plane or vertical direction parallel to the growth direction is the most relevant concern, especially for SL material where anisotropic transport is expected. Assessing vertical transport in SLs has been accomplished using a variety of methodologies. An early work on p-type InAs/GaSb using electron beam induced current in combination with minority carrier lifetime measurements determined the dominant electron carrier vertical mobility dependence on temperature [21]. Current-voltage and minority carrier lifetime measurements on a heterojunction bipolar transistor were then used to determine the vertical hole transport in LWIR InAs/InAsSb T2SLs that was dominated by hopping transport due to carrier localization [22]. Both electron and hole vertical transport in MWIR n-type InAs/InAsSb T2SLs was simultaneously obtained by Casias *et al.* using a unique vertical magneto-transport device structure (metal-semiconductor-metal), in combination with QMSA and the in-plane transport measurements presented in this paper [23]. Finally, similar vertical hole mobility results as those were then recently obtained from modelling of quantum efficiency measurements on an nBn IR detector with an n-type InAs/InAsSb T2SL absorber, again in combination with minority carrier lifetime measurements [24].

3. Experimental

Conventional Hall effect and resistivity measurements and analysis at a single magnetic field are only accurate if a single carrier species is contributing to conduction in the sample. Once additional carrier species are present, the transport becomes mixed, and possibly ambipolar, and the conventional approach only produces an average value of all the carriers concentration and mobilities. Narrow-gap IR III-V materials, such as the bulk InAsSb alloy and InAs/InAsSb T2SLs used in this work, are typically plagued by the presence of additional carriers that contribute to conduction (e.g., surface electrons, minority carriers, interface carriers, etc.) [20]. Additionally, these materials are typically grown lattice-matched to highly conductive GaSb substrates, thus, to accurately assess the carrier concentration and mobility in these materials a variable, a high magnetic field magneto-transport measurement in combination with a least-squares multi-carrier fitting (MCF) procedure needs to be implemented.

Multi-carrier conduction is characterised by a conductivity tensor which has longitudinal and transverse components, σ_{xx} and σ_{xy} , given by

$$\sigma_{xx}(B) = \sum_{i=1}^N \frac{q_i n_i \mu_i}{1 + \mu_i^2 B^2} \quad (1)$$

$$\sigma_{xy}(B) = \sum_{i=1}^N \frac{q_i n_i \mu_i^2 B}{1 + \mu_i^2 B^2}, \quad (2)$$

where q_i is the signed charge, n_i is the carrier concentration, and μ_i is the mobility of the i^{th} carrier species, B is the magnetic field applied transversely to the carrier motion, and N is the total number of carrier species. Inspecting (1) and (2), the conduction contribution from the i^{th} carrier species becomes quenched as $\mu_i B \gg 1$ [25]. Thus, higher mobility carriers, such as lighter electrons, are quenched at lower B -fields while higher B -fields are required to quench lower mobility carriers, such as heavier holes. This behaviour necessitates the use of high magnetic fields up to 10 T to probe the conduction.

The measured Hall coefficient $R_H(B)$ and the longitudinal sheet resistivity $\rho_s(B)$ are related to the conductivity components according to [26, 27]

$$\rho_{xx}(B) = \frac{\rho_s(B)}{\rho_s(B)^2 + R_H(B)^2 B^2} \quad (3)$$

$$\rho_{xy}(B) = \frac{R_H(B) B}{\rho_s(B)^2 + R_H(B)^2 B^2}. \quad (4)$$

Thus, in practice, the measured $\rho_s(B)$ and $R_H(B)$ are used to determine experimental values for $\sigma_{xx}^{\text{exp}}(B)$ and $\sigma_{xy}^{\text{exp}}(B)$ and then a least-square fit with a pre-set number of carriers N is performed using

$$\chi^2 = \sum_{i=1}^M \left[\left(\sigma_{xx}^{\text{exp}}(B_i) - \sum_{j=1}^N \sigma_{xx}^j(B_i) \right)^2 + \left(\sigma_{xy}^{\text{exp}}(B_i) - \sum_{j=1}^N \sigma_{xy}^j(B_i) \right)^2 \right], \quad (5)$$

where M is the total number of discrete magnetic fields used for measurements [28]. Here, (μ_j, q_j, n_j) of each carrier are the fitting parameters.

In this work, Hall coefficient and resistivity measurements are taken on 4 different samples: (1) non-intentionally doped (*NID*) InAs_{0.91}Sb_{0.09} alloy; (2) Si-doped, n-type $1 \cdot 10^{16} \text{ cm}^{-3}$ InAs_{0.91}Sb_{0.09} alloy; (3) *NID* InAs/InAs_{0.65}Sb_{0.35} T2SL; and (4) Si-doped, n-type $1 \cdot 10^{16} \text{ cm}^{-3}$ InAs/InAs_{0.65}Sb_{0.35} T2SL. Schematics of the fabricated samples in the van der Pauw (VDP) configuration are shown in Fig. 1.

These samples are grown by molecular beam epitaxy (MBE) on n-type (Te-doped) GaSb substrates. As Fig. 1 shows, for both sets of samples, a 2 μm thick lattice-matched active region, either *NID* or Si-doped n-type $1 \cdot 10^{16} \text{ cm}^{-3}$, is grown on top of a 0.01 μm thick undoped GaSb buffer. This is in turn grown on a 0.5 μm thick, undoped AlAs_{0.08}Sb_{0.92} insulating layer that is grown directly on the substrate material. The wide-bandgap AlAsSb insulating layer is present to eliminate substrate

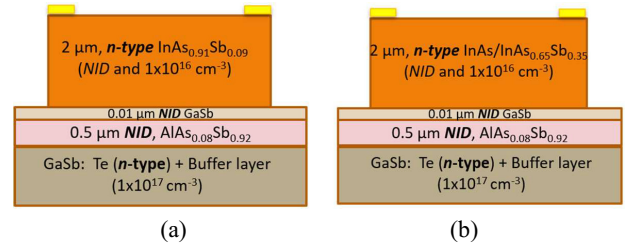


Fig. 1. Schematics of the mesa-etched, van der Pauw (VDP) InAs_{0.91}Sb_{0.09} alloy (a) and InAs/InAs_{0.65}Sb_{0.35} T2SL sample (b) sets showing the sample structure and fabricated device configuration. Active regions in each sample were either *NID* or Si-doped n-type $1 \cdot 10^{16} \text{ cm}^{-3}$.

conduction, as described in Refs. 15 and 16, and limit conduction to the 2 μm thick active regions. The GaSb buffer layer is necessary to achieve sufficient, although not unexpected state of the art, minority carrier lifetimes in the InAsSb-based active regions, which were severely degraded when the thin GaSb interface treatment was not present. The chosen alloy concentration InAs_{0.91}Sb_{0.09} and the InAs/InAs_{0.65}Sb_{0.35} T2SL are both lattice-matched (or strain-balanced) to the GaSb substrate. Standard material characterisation of samples, the details of which are provided in Ref. 13, from each wafer is performed including: X-ray diffraction, Nomarski imaging, photoluminescence (PL), and minority carrier lifetime. Summarising, X-ray diffraction determined InAs/InAs_{0.65}Sb_{0.35} T2SL samples are precisely strain-balanced, while the InAs_{0.91}Sb_{0.09} alloy is compressively strained by 130 arcsec. Nomarski imaging showed samples had clean surface morphology with no defects over large lateral distances. PL and minority carrier lifetime results for each sample are summarised in Table 1.

Table 1.
Optoelectronic properties of each sample.

Structure	Doping	Lifetime at 100 K (μs)	PL at 80 K (μm)
InAs _{0.91} Sb _{0.09}	<i>NID</i>	0.13	3.88
InAs _{0.91} Sb _{0.09}	$1 \cdot 10^{16}$	0.05	3.91
InAs/InAs _{0.65} Sb _{0.35}	<i>NID</i>	1.45	5.14
InAs/InAs _{0.65} Sb _{0.35}	$1 \cdot 10^{16}$	0.25	5.20

For transport measurements, standard contact photolithography followed by wet-etching is used to define 5 mm \times 5 mm square mesas in VDP configuration. Wet-etching using a citric acid-based etch (citric acid: H₂O₂(30%) = 5:1) is done at room temperature. The resulting etch is confirmed to be 2 μm by stylus profilemetry on all samples. A 30 sec native oxide etch in dilute hydrochloric acid solution (HCl:H₂O = 1:20) is then performed. Following this, 300 μm square contacts with a 25 μm offset from the mesa edge are lithographically defined and Ti (500 \AA)/Pt (500 \AA)/Au (3000 \AA) contact metal is evaporated, and contacts are formed via a metal lift-off process. Samples are then packaged in leadless chip carriers and wire bonded. Ohmic contacts are verified for each sample by current-voltage measurements along each contact pair (i.e., $R_{1212} = R_{1+L-V+V-}$) for each temperature of interest.

Variable-field, variable-temperature Hall effect and resistivity measurements are performed on a Lakeshore

9509 Hall Measurement System (HMS) equipped with a 9 T superconducting magnet at a drive current of 100 μA . Current reversal, magnetic field B reversal, and both Hall configurations are used to eliminate sample-induced measurement errors, and temperatures are varied from 15 K to 390 K. The HMS generates the sheet resistivity $\rho_s(B)$ and the Hall coefficient $R_H(B)$ values as a function of magnetic field at each temperature. To examine whether multi-carrier conduction is present, plots of the measured $\rho_s(B)$ vs. B are inspected. For single carrier conduction, the magneto-resistivity is expected to be independent of B and given by

$$\rho_s(B) = \rho_s(0) = \frac{1}{\sigma_{xx}(0)} = \frac{1}{qn\mu}, \quad (6)$$

according to (1) and (3) for $N = 1$.

Once multi-carrier conduction is confirmed, then the measured $\rho_s(B)$ and $R_H(B)$ are input in the Lakeshore MCF analysis tool. This tool, in turn, generates $\sigma_{xx}^{exp}(B)$ and $\sigma_{xy}^{exp}(B)$, according to (3) and (4), and then performs the least-square fitting using (5). From that fitting, a sheet carrier concentration n_i or p_i and mobility μ_i are determined for each i^{th} carrier species [28]. From n_i and μ_i , the sheet conductivity of each carrier species $\sigma_i = qn_i\mu_i$ is calculated.

Finally, to understanding the source and/or location of each carrier species determined by the MCF routine, three different analysis approaches are taken. First, to determine which carriers are the surface carriers, the samples are dipped in a 5.25% sodium hypochlorite (NaClO) solution and rinsed in deionized water [29]. This straightforward procedure modifies the sample surface sufficiently that the transport properties of the surface carriers change without impacting on the transport of the other carrier species. Second, as discussed above, there is a GaSb buffer layer between active region and an AlAsSb insulating layer in each sample, which has the potential to trap carriers and act as a quantum well. This possibility was investigated by modelling each sample with NRL MULTIBANDS® and comparing those results to the MCF results. Finally, the MCF results are also compared to some previous results [20].

4. Results and analysis

An example of the NRL MULTIBANDS® modelling results is shown in Fig. 2 for the *NID* InAsSb sample. Plots (a) and (b) are the expected band diagram and carrier concentrations. A surface accumulation concentration of $5.0 \cdot 10^{17} \text{ cm}^{-3}$ was assumed for all samples, based on several references as described in section 5.4.1 of Ref. 13. All four samples are also predicted to have electron and hole wells at the interface region between the active layer and the GaSb buffer layer. A summary of the predictions for the interface electron and hole sheet carrier concentrations in these wells is given in Table 2. The predicted sheet concentrations for all samples were in the range of $\sim 10^{12} \text{ cm}^{-2}$ at 300 K.

Example measurements of the sheet carrier resistivity $\rho_s(B)$ at 77 K and 300 K for all four samples are shown in Fig. 3. These data confirmed the presence of multi-carrier conduction in all four samples and, therefore, the necessity of using MCF. Additionally, $\rho_s(B)$ appeared to generally

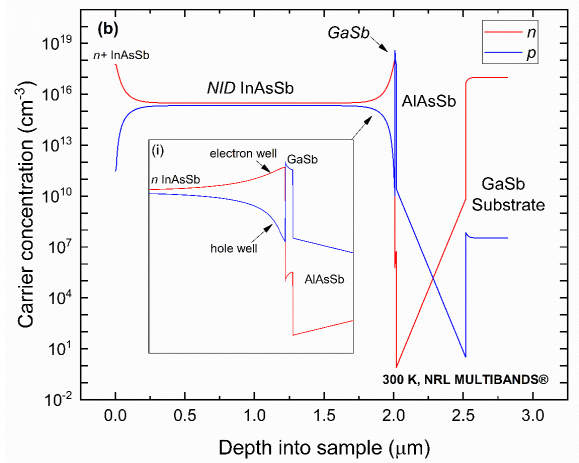
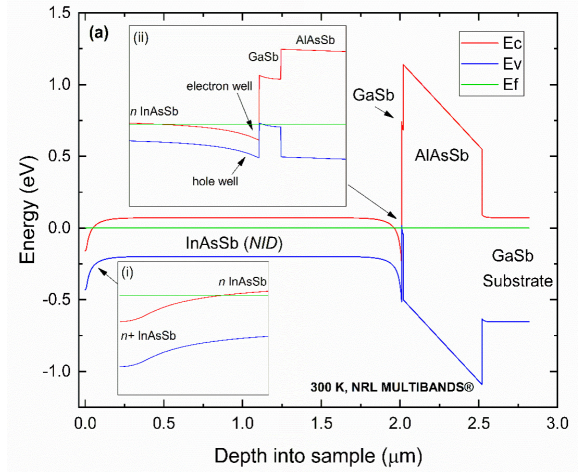


Fig. 2. NRL MULTIBANDS® modelling of the *NID* InAsSb sample energy band diagram (a) and carrier concentration vs. depth at 300 K (b). Inset plots in (a) and (b) show the interface electron and hole wells.

Table 2.
Interface carrier concentration
from NRL MULTIBANDS® at 300 K.

Sample	Interface electron sheet concentration (10^{12} cm^{-2})	Interface hole sheet concentration (10^{12} cm^{-2})
<i>NID</i> InAs _{0.91} Sb _{0.09}	1.6	1.2
Si-doped InAs _{0.91} Sb _{0.09}	1.7	1.2
<i>NID</i> InAs/InAs _{0.65} Sb _{0.35}	2.2	1.4
Si-doped InAs/InAs _{0.65} Sb _{0.35}	2.2	1.4

decrease with increasing temperature and Si-doping; both trends are likely due to increased carrier concentration. Results of the MCF and analysis for each sample are given in sections 4 through 4.

4.1. *NID* and Si-doped InAs_{0.91}Sb_{0.09}

The transport results for the *NID* InAs_{0.91}Sb_{0.09} sample are shown in Fig. 4. Results here indicated the presence of 4 carriers including: (1) bulk electrons; (2) interface electrons; (3) surface electrons; and (4) minority holes. Similar results are obtained for the Si-doped InAs_{0.91}Sb_{0.09} sample (not shown). Following the procedure discussed in

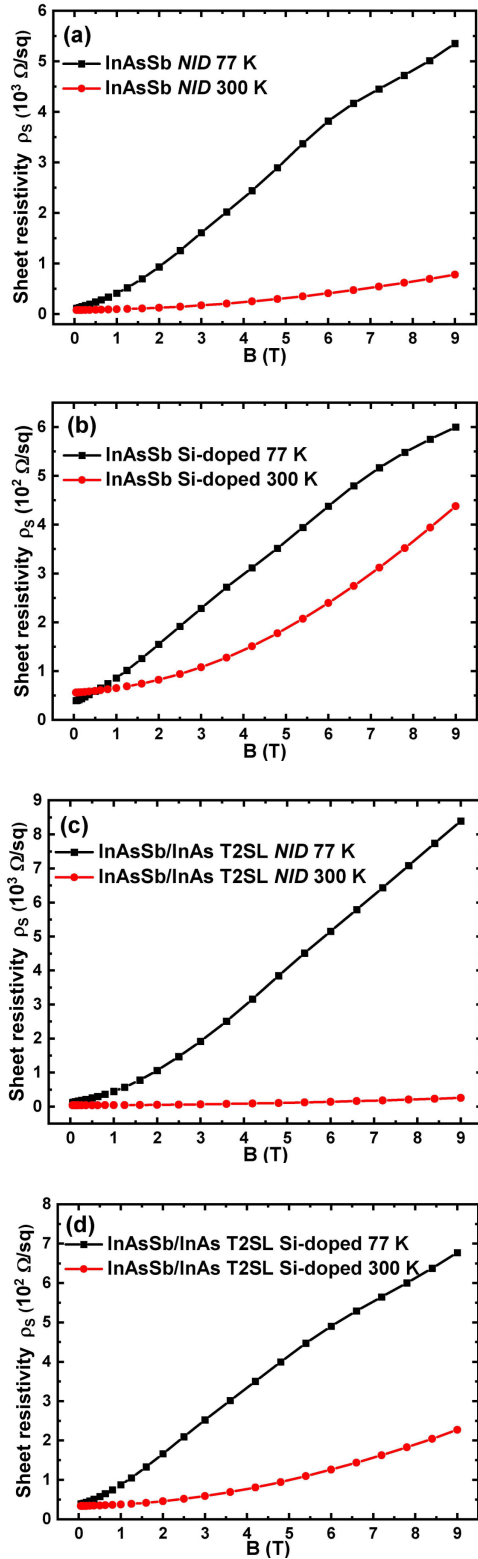


Fig. 3. Plots of $\rho_s(B)$ vs. B for: *NID* InAs_{0.91}Sb_{0.09} (a); Si-doped InAs_{0.91}Sb_{0.09} (b); *NID* InAs/InAs T2SL (c); and *NID* InAs/InAs T2SL exhibiting multi-carrier conduction (d).

section 3, carrier $e3$ was determined to be surface electrons by dipping the sample in NaClO and observing a change in its mobility alone. At 20 K, $e3$ contributed 14% of the total conduction where 20 K is a convenient temperature for comparison sake. In both the *NID* and Si-doped alloy samples, $e3$ mobility and sheet concentration were insensitive to temperature.

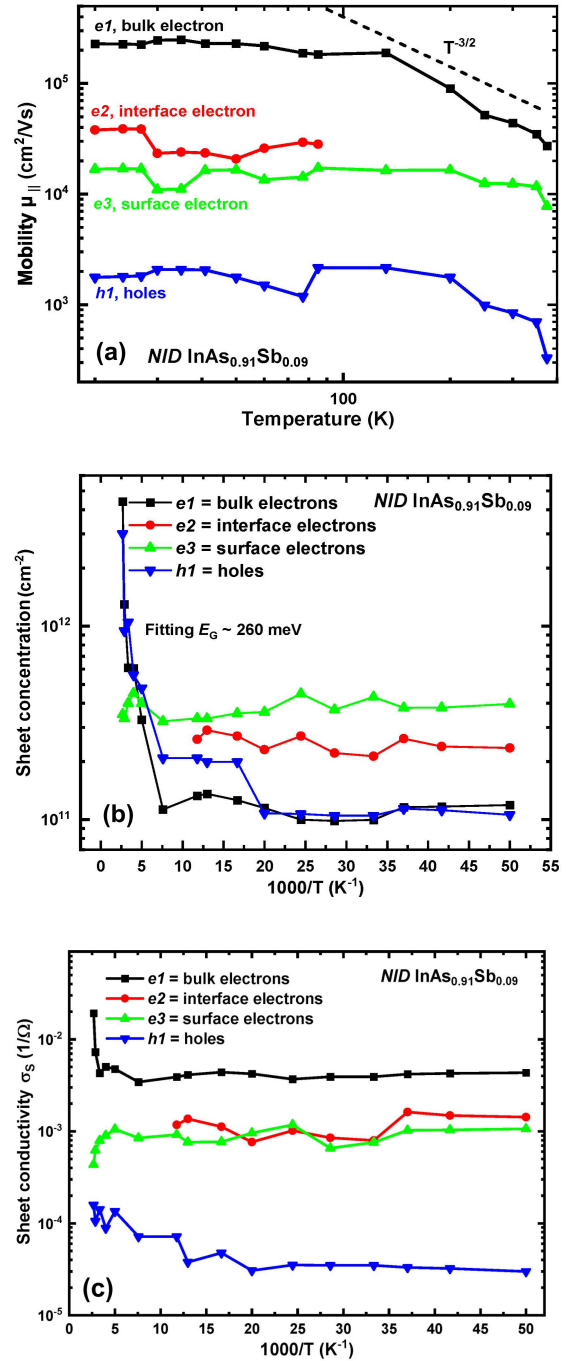


Fig. 4. Temperature-dependence of the *NID* InAs_{0.91}Sb_{0.09} mobility (a); sheet concentration (b); and sheet conductivity (c). 4 carriers are resolved by MCF.

Carrier $e1$ contributed 64% of the conduction at 20 K and had the highest mobility. $\sim 1.9 \cdot 10^5$ cm²/Vs at 77 K, across the entire temperature range. Moreover, μ_{e1} demonstrated a bulk-like $T^{-3/2}$ -dependence for $T > 130$ K, indicative of lattice vibration limited mobility, and n_{e1} showed a clear intrinsic region, confirming the bulk-like nature of carrier $e1$. From a fitting of its sheet concentration n_{e1} , an activation energy of 260 meV is obtained. A background concentration of $\sim 5 \cdot 10^{14}$ cm⁻³ is calculated from n_{e1} in the freeze-out region $T < 50$ K. Notably, in the Si-doped alloy sample, the freeze-out region occurs at $T < 30$ K and $e1$ mobility dropped by $2 \times$ to $\sim 9 \cdot 10^4$ cm²/Vs, which suggests it is limited by ionized impurity scattering for $T < 130$ K.

Carrier $e2$ contributed 21% of the conduction at 20 K and both μ_{e2} and n_{e2} are insensitive to temperature. The sheet concentration n_{e2} is comparable to the NRL MULTIBANDS® modelling results in Table 2, suggesting carrier $e2$ is the interface electron.

Finally, carrier $h1$ contributed <1% of the conduction at 20 K in the *NID* alloy sample and both μ_{h1} and n_{h1} exhibit bulk-like qualities to their temperature dependence. In the Si-doped alloy sample, however, $h1$ mobility is insensitive to temperature, and it is more identifiable as an interface hole. Thus, the data suggests the MCF did not clearly resolve carrier $h1$ in either of these samples and $h1$ may have represented some combination of interface and bulk holes, where *bulk* refers to the location of the carriers which are strongly localized in the growth direction. Summarising, both the *NID* and Si-doped InAs_{0.91}Sb_{0.09} alloy samples appeared strongly n-type and clearly presented multi-carrier conduction with 4 carriers being resolved by MCF in each.

4.2. *NID* and Si-doped InAs/InAs_{0.65}Sb_{0.35} T2SL

Transport results for the *NID* InAs/InAs_{0.65}Sb_{0.35} T2SL sample are shown in Fig. 5. Here, MCF now clearly resolves 5 distinct carriers contributing to conduction. This again included: (1) bulk electrons; (2) interface electrons; and (3) surface electrons. Unique to the T2SL samples, it now clearly includes (4) bulk minority holes; and (5) interface holes, separately. Again, largely similar results as these are obtained for the Si-doped InAs/InAs_{0.65}Sb_{0.35} T2SL sample (not shown). For the T2SL carrier $e3$ contributed 13% of the conduction at 20 K and is again identified as surface electrons by dipping the sample in NaClO and observing a change in its mobility alone. In both the *NID* and Si-doped T2SL samples, $e3$ mobility and sheet concentration are again insensitive to temperature, as expected for surface electrons.

Carrier $e1$ in the *NID* T2SL sample contributed 80% of the conduction at 20 K and had the highest mobility, $\sim 2.6 \cdot 10^5$ cm²/Vs at 77 K, over the entire temperature range. Carrier $h1$ contributed 7% of the conduction at 20 K, with a mobility of $\sim 5.5 \cdot 10^3$ cm²/Vs at 77 K. In the Si-doped T2SL sample, the $e1$ and $h1$ mobilities at 77 K are again lower by $\sim 2\times$, at $\sim 8.9 \cdot 10^4$ cm²/Vs and $\sim 1.6 \cdot 10^5$ cm²/Vs, respectively, suggesting ionized impurity scattering dominated here. For $T > 130$ K both μ_{e1} and μ_{h1} exhibited clear bulk-like $T^{-3/2}$ -dependence indicative of lattice vibration limited mobility. Both n_{e1} and p_{h1} also exhibit clear intrinsic regions, which together further validates their bulk-like natures. From a fitting of sheet concentration n_{e1} an activation energy of 235 meV is obtained. From n_{e1} and p_{h1} , a background electron concentration of $\sim 5 \cdot 10^{14}$ cm⁻³ and a higher background hole concentration of $\sim 2 \cdot 10^{15}$ cm⁻³ are calculated in the region $T < 200$ K. Notably, in the Si-doped InAs/InAs_{0.65}Sb_{0.35} T2SL n_{e1} results clear extrinsic and freeze-out regions are observed below 200 K and 20 K, respectively.

Carrier $e2$ was unresolved by the MCL and thus did not contribute to the conduction below 30 K. Above that, both μ_{e2} and n_{e2} are roughly independent of temperature. The sheet concentration n_{e2} is again comparable to the NRL

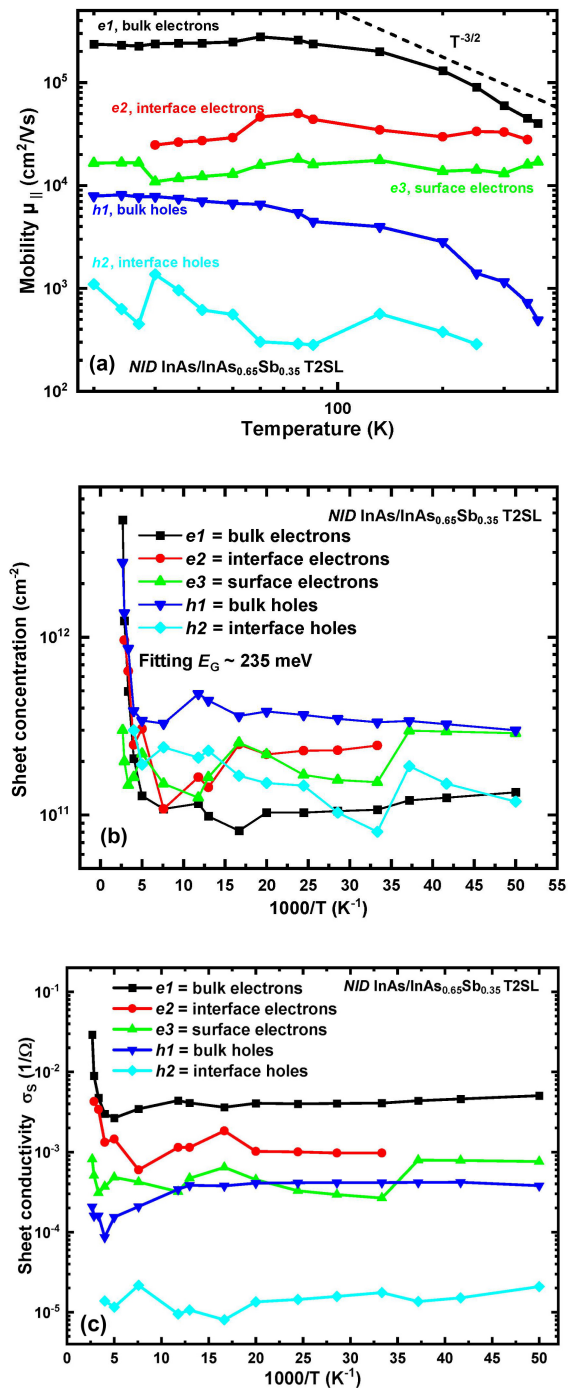


Fig. 5. Temperature-dependence of the *NID* InAs/ InAs_{0.65}Sb_{0.35} T2SL mobility (a); sheet concentration (b); and sheet conductivity (c). 5 carriers are resolved by MCF.

MULTIBANDS® modelling results in Table 2, which suggests carrier $e2$ in the T2SL samples is also an interface electron.

Finally, carrier $h2$ also contributed <1% of the conduction at 20 K and both μ_{h2} and n_{h2} are roughly independent of temperature, which suggests carrier $h2$ is the interface hole population. Summarising, both the *NID* and Si-doped InAs/InAs_{0.65}Sb_{0.35} T2SL samples appear strongly n-type and clearly presented multi-carrier conduction with 5 carriers being resolved by MCF in each, including clearly resolved bulk and interface holes.

5. Conclusions

Temperature- and magnetic-field-dependent measurements, MCF, and NRL MULTIBANDS® modelling are all used to identify the different carrier species contributing to the conduction in III-V MWIR materials. Transport in the *NID* and Si-doped $1 \cdot 10^{16} \text{ cm}^{-3}$ InAs_{0.91}Sb_{0.09} alloy and InAs/InAs_{0.65}Sb_{0.35} T2SL samples are found to be roughly similar with conduction dominated in each sample by carrier *e1*, identified to be bulk electrons. All samples also exhibited carriers *e2* and *e3*, identified to be interface and surface electrons, respectively. The main exception to the similarity in their transport is in the amount of hole conduction. In the InAs/InAs_{0.65}Sb_{0.35} T2SL samples, 2 carriers, *h1* and *h2*, the bulk and interface holes, respectively, were clearly identified compared to the InAs_{0.91}Sb_{0.09} alloy samples, where only an *h1* carrier was resolved. The *h1* carrier in the *NID* T2SL also contributed nearly 7% of the conduction at 20 K, while in the *NID* alloy sample *h1* contributed <1%. Finally, the alloy and T2SL materials also differ in their background carrier concentration, which is dominated by *h1* in the latter while its overall conduction is still strongly n-type. Finally, notably the mobility results for *e1* and *h1* in Fig. 5(a) are previously used in combination with transport measurements on a vertical structure with a similar InAs/InAs_{0.65}Sb_{0.35} T2SL active region to accurately determine the vertical mobility of electrons and holes [23] As mentioned in section 1, these transport results allow the optimization of improved detector materials and designs.

Authors' statement

The individual contribution of each author is as follows. The research concept and design, L.K.C., P.T.W., and P.C.G.; collection and/or assembly of data, L.K.C.; data analysis and interpretation, L.K.C. and C.P.M.; writing the article, C.P.M.; critical revision of the article, P.T.W., G.A.U-M, and S.K.; final approval of article, V.M.C., L.F., and G.B.

Acknowledgements

The views expressed are those of the author and do not necessarily reflect the official policy or position of the Dept. of the Air Force, the Dept. of Defense, or the U.S. government. This work was performed in part at CINT, an Office of Science User Facility operated for the U.S. DOE Office of Science. Sandia National Laboratories is a multi-mission lab managed and operated by NT&ES of Sandia, LLC, a wholly owned subsidiary of Honeywell International Inc., for the US DOE's NNSA under Contract No. DE-NA0003525.

References

- Lee, D. *et al.* Law 19: The ultimate photodiode performance metric. *Proc. SPIE* **11407**, 114070X (2020). <https://doi.org/10.1117/12.2564902>
- Lee, D. *et al.* High-operating temperature HgCdTe: a vision for the near future. *J. Electron. Mater.* **45**, 4587–4595 (2016). <https://doi.org/10.1007/s11664-016-4566-6>
- Elliott, T. Recollections of MCT work in the UK at Malvern and Southampton. *Proc. SPIE* **7298**, 7298M (2009). <https://doi.org/10.1117/12.820214>
- European Union. *Directive 2011/65/EU of The European Parliament and of the Council of 8 June 2011 on The Restriction of The Use of Certain Hazardous Substances in Electrical and Electronic Equipment.* (updated in 2022). <http://data.europa.eu/eli/dir/2011/65/2022-10-01> (2022).
- Roberts, T. G. Space Launch to Low Earth Orbit: How Much Does it Cost? <https://aerospace.csis.org/data/space-launch-to-low-earth-orbit-how-much-does-it-cost/> (2022).
- Kosiak, S. Small Satellites in the Emerging Space Environment: Implications for U.S. National Security-Related Space Plans and Programs. Center for a New American Security, 2019.
- Rogalski, A. HgCdTe Photodetectors. in *Mid-infrared Optoelectronics. Materials, Devices, and Applications* (eds. Tournie, E. & Cerutti, L.) 235–335 (Elsevier, Duxford, 2020).
- Maimon, S. & Wicks, G. W. nBn detector, an infrared detector with reduced dark current and higher operating temperature. *Appl. Phys. Lett.* **89**, 151109 (2006). <https://doi.org/10.1063/1.2360235>
- Rogalski, A., Martyniuk, P., Kopytko, M., Madejczyk, P. & Krishna, S. InAsSb-based infrared photodetectors: thirty years later on. *Sensors* **20**, 7047 (2020). <https://doi.org/10.3390/s20247047>
- Tennant, W. E. "Rule 07" Revisited: still a good heuristic predictor of p/n HgCdTe photodiode performance? *J. Electron. Mater.* **39**, 1030–1035 (2010). <https://doi.org/10.1007/s11664-010-1084-9>
- Morath, C. P., Cowan, V. M., Treider, L. A., Jenkins, G. D. & Hubbs, J. E. Proton irradiation effects on the performance of III-V-based, unipolar barrier infrared detectors. *IEEE Trans. Nucl. Sci.* **62**, 512–519 (2015). <https://doi.org/10.1109/TNS.2015.2392695>
- Jenkins, G. D., Morath, C. P. & Cowan, V. M. Empirical study of the disparity in radiation tolerance of the minority-carrier lifetime between II-VI and III-V MWIR detector technologies for space applications. *J. Electron. Mater.* **46**, 5405–5410 (2017). <https://doi.org/10.1007/s11664-017-5628-0>
- Casias, L. K. Transport in Mid-Wavelength Infrared p- and n- InAsSb and InAs/InAsSb Type-II Strained Layer Superlattices for Infrared Detection. (University of New Mexico, 2019).
- Hoffman, C. A., Meyer, J. R., Youngdale, E. R. & Bartoli, F. J. Interface roughness scattering in semiconducting and semimetallic InAs/GaInSb. *Appl. Phys. Lett.* **63**, 2210 (1993). <https://doi.org/10.1063/1.110800>
- Rao, T. V. Quantitative mobility spectrum analysis of carriers in GaSb/InAs/GaSb superlattice. *J. Vac. Sci. Technol. B* **26**, 1081–1083 (2008). <https://doi.org/10.1116/1.2839641>
- Szmulowicz, F., Elhamri, S., Haugan, H. J., Brown, G. J. and Mitchel, W. C. Carrier mobility as a function of carrier density in type-II InAs/GaSb superlattices. *J. Appl. Phys.* **105**, 074303 (2009). <https://doi.org/10.1063/1.3103281>
- Cervera, C. *et al.* Transport measurements on InAs/GaSb superlattice structures for mid-infrared photodiode. *J. Phys. Conf. Ser.* **193**, 012030 (2009). <https://doi.org/10.1088/1742-6596/193/1/012030>
- Szmulowicz, F., Haugan, H.G., Elhamri, S., Brown, G.J. & Mitchel, W.C. Transport studies of MBE-grown InAs/GaSb superlattices. *Opto-Electron. Rev.* **18**, 267–270 (2010). <https://doi.org/10.2478/s11772-010-1027-6>
- Brown, A.E. *et al.* Characterization of n-type and p-type long-wave InAs/InAsSb superlattices. *J. Electron. Mater.* **46**, 5367–5373 (2017). <https://doi.org/10.1007/s11664-017-5621-7>
- Casias, L.K. *et al.* Carrier concentration and transport in Be-doped InAsSb for infrared sensing applications. *Proc. SPIE* **10624**, 106240M (2018). <https://doi.org/10.1117/12.2305431>
- Taghipour, Z. *et al.* Temperature-dependent minority carrier mobility in p-type InAs/GaSb type-II-superlattice photodiodes. *Phys. Rev. Appl.* **11**, 024047 (2019). <https://doi.org/10.1103/PhysRevApplied.11.024047>
- Olson, B.V. *et al.* Vertical hole transport and carrier localization in InAs/InAsSb type-II superlattice heterojunction bipolar transistors. *Phys. Rev. Appl.* **7**, 024016 (2017). <https://doi.org/10.1103/PhysRevApplied.7.024016>
- Casias, L.K. *et al.* Vertical carrier transport in strain-balanced InAs/InAsSb type-II superlattice material. *Appl. Phys. Lett.* **116**, 182109 (2020). <https://doi.org/10.1063/1.5144079>
- Arounassalame, V. *et al.* Anisotropic transport investigation through different etching depths in InAs/InAsSb T2SL barrier midwave infrared detector. *Infrared Phys. Technol.* **126**, 104315 (2022). <https://doi.org/10.1016/j.infrared.2022.104315>

- [25] Antoszewski, J., Seymour, D.J., Faraone, L., Meyer, J.R. & Hoffman, C.A. Magneto-transport characterization using quantitative mobility-spectrum analysis (QMSA). *J. Electron. Mater.* **24**, 1255–1262 (1995). <https://doi.org/10.1007/BF02653082>
- [26] Beck, W.A. & Andersen, J.R. Determination of electrical transport properties using a novel magnetic field-dependent Hall technique. *J. Appl. Phys.* **62**, 541–554 (1987). <https://doi.org/10.1063/1.339780>
- [27] Umana-Membreno, G. A. Investigation of multicarrier transport in LPE-Grown HgCdTe layers. *J. Electr. Mat.* **39**, 1023–1029 (2010). <https://doi.org/10.1007/s11664-010-1086-7>
- [28] Du, G. et al. Characterizing multi-carrier devices with quantitative mobility spectrum analysis and variable field hall measurements. *Jpn. J. Appl. Phys.* **41**, 1055–1058 (2002). <https://doi.org/10.1143/JJAP.41.1055>
- [29] Svensson, S.P. et al. Background and interface electron populations in InAsSb. *Semicond. Sci. Technol.* **30**, 035018 (2015). <https://doi.org/10.1088/0268-1242/30/3/035018>